Journal of Zhejiang University-SCIENCE A (Applied Physics & Engineering)
ISSN 1673-565X (Print); ISSN 1862-1775 (Online)
www.jzus.zju.edu.cn; www.springerlink.com
E-mail: jzus@zju.edu.cn

Numerical study on the flow field characteristics of the new high-speed maglev train in open air*

Peng ZHOU, Tian LI, Chun-fa ZHAO, Ji-ye ZHANG†‡

State Key Laboratory of Traction Power, Southwest Jiaotong University, Chengdu 610031, China

†E-mail: jyzhang@home.swjtu.edu.cn

Received Aug. 22, 2019; Revision accepted Mar. 11, 2020; Crosschecked Apr. 14, 2020

Abstract: With the increasing demand of higher travelling speed, a new streamlined high-speed maglev train has been designed to reach a speed of 600 km/h. To better capture the flow field structures around the maglev train, an improved delayed detached eddy simulation (IDDES) is adopted to model the turbulence. Results show that the new maglev train has good aerodynamic load performance such as small drag coefficient contributing to energy conservation. The main frequencies of aerodynamic forces for each car have a scattered distribution. There are two pairs of counter-rotating large vortices in the non-streamlined part of the train that make the boundary layer thicker. Many high-intensity vortices are distributed in the narrow space between skirt plates or train floor and track. In the gap between the train floor and track (except near the tail car nose), the main frequency of vortex shedding remains constant and its strength increases exponentially in the streamwise direction. In the wake, the counter-rotating vortices gradually expand and reproduce some small vortices that move downward. The vortex has quite random and complex frequency-domain distribution characteristics in the wake. The maximum time-averaged velocity of the slipstream occurs near the nose of the head car, based on which, the track-side safety domain is divided.

Key words: Maglev train; High-speed; Improved delayed detached eddy simulation (IDDES); Aerodynamic load; Vortex; Time-averaged slipstream

https://doi.org/10.1631/jzus.A1900412 **CLC number:** U237

1 Introduction

With the increase of demand for travel, researchers have focused on achieving faster, safer, more comfortable, and more energy-saving train operation (Zhang et al., 2017; Miao et al., 2019; Zhou et al., 2020). Many countries such as Germany, Japan, Korea, and China have therefore begun to focus on studies of high-speed maglev trains (Ono et al., 2002; Yan, 2007; Lee et al., 2014). The maglev train is a special transportation vehicle with a non-contact and non-wearing levitation, driven by electromagnetic, electrodynamic, or super-conducting principles (Deng et al., 2019). Unlike the widely used wheel-rail train in this day and age, the maglev train has much better performance in such aspects as energy consumption, vibration noise, and safety (Lee et al., 2006). The maglev train can efficiently avoid derailment due to no wheel-rail adhesion, and provides a probable route for improving train speed further. Even if the maglev train could realize a higher travel speed, such as 600 km/h, high-speed motion might cause some key aerodynamic problems which deserve attention.

Compared with the high-speed wheel-rail train, studies on the aerodynamics of the high-speed maglev train are fewer because of fewer engineering applications. Typically, some aerodynamic numerical analyses and full-scale tests have been carried out on the

‡ Corresponding author

* Project supported by the National Natural Science Foundation of China (No. 51605397), the National Key R&D Program of China (No. 2016YFB1200602-15), and the Sichuan Provincial Science and Technology Support Program (No. 2019YJ0227), China

ORCID: Peng ZHOU, https://orcid.org/0000-0002-0610-8149

TR08 maglev train running on the Shanghai maglev line with different running speeds (Bi et al., 2004, 2005; Li et al., 2006). These indicate that the simulation results from the numerical simulation algorithm considering compressibility are in good agreement with the experimental data. For the high-speed maglev train, the suspension gap is of great concern for operational safety. Maglev vehicles made up of different suspension principles have different suspension gap requirements. The effect of the suspension gap on the aerodynamic characteristics of the various maglev trains is studied based on the k-ε turbulence model (Li et al., 2004), which indicates that it has little effect on the train drag, but more on the train lift. In the aspect of shape optimization, the flat shuttle head shape with the longer streamline length can effectively reduce aerodynamic drag and weaken the shock effect during the intersection process of the two trains. Huang et al. (2019) reproduced the intersection process of a maglev train at the speed of 430 km/h by the sliding mesh method, and obtained the safe distance beside the track. Jia and Mei (2018) established a 1D compressible unsteady non-isentropic flow model to study the pressure waves generated by the high-speed maglev train passing through the tunnel. This cannot represent the 3D aerodynamic effect of the high-speed maglev train because of dimension limitations. Chen (2018) demonstrated in detail that the aerodynamic performance of the new streamlined Transrapid (TR) train is better than that of the TR08 train in the intersection process by the numerical method.

However, the complex unsteady flow characteristics induced by the high-speed maglev train, especially the vortex structures, have not been clarified well in previous studies. In this study, the unsteady aerodynamic characteristics of a simplified new maglev train running at 600 km/h in open air are studied by the improved delayed detached eddy simulation (IDDES) method, which has been applied to much high-speed train engineering successfully. Using the IDDES method, the aerodynamic force, train surface pressure, and slipstream velocity distributions of the 1/8th scale CRH3 model are obtained, and are in good agreement with wind tunnel test results (Xia et al., 2017). Similarly, the numerical slipstream pressures induced by the full-scale CRH2C model are also in good agreement with test results on the Wuhan-Guangzhou high-speed railway line (Wang et al., 2019). More importantly, this method is often used to study the unsteady flow structure around the train, especially the wake topology (Wang et al., 2018; Li et al., 2019). Based on the successful experience of predicting the unsteady flow by the IDDES method, some flow problems caused by the high-speed maglev train, such as vortex shedding frequency in wake and trackside safety domain, can be revealed in depth. The findings in the study are expected to lay a good foundation for the development and operation of the high-speed maglev train in China.

In this study, some numerical simulation details, such as the new maglev train model, the mesh generation, the solver description, and the IDDES method, are introduced. Then, the numerical verification and flow field characteristics, such as the unsteady aerodynamic forces, the boundary layer development, the vortex shedding characteristics, and the time-averaged slipstream, are discussed.

2 Numerical

2.1 Geometric model

Compared with the TR08 train running on the Shanghai maglev demonstration line (Liu et al., 2006), the streamlined length of the new TR train is up to about 16 m. The simplified maglev train model consists of the head car (HC), mid car (MC), and tail car (TC), as shown in Fig. 1. The totally enclosed windshield of 250 mm length is adopted to connect the adjacent cars. Given the small suspension gap of about 10 mm, the distance H from the train top to the track bottom is regarded as the characteristic height of the model, which is about 4.55 m. The whole train length is about 17.8H. The lengths of the streamlined and non-streamlined cars are 6.2H and 5.4H, respectively. The height and width of the whole maglev train are 0.9H and 0.8H, respectively.

2.2 Computational domain and boundary conditions

The motion of the maglev train along the $+x$ direction is realized by the relative motion principle. The whole computational domain is shown in Fig. 2. In order to reduce the computational scale, the complicated bridge structures are neglected. The track height that is the vertical distance from the track

bottom to the ground is 5 m and its length runs through the whole domain in the streamwise direction. The nose tips of HC and TC are about 10H and 18H from the pressure inlet and the pressure outlet, respectively, ensuring a sufficient development of the flow field. The distance between the track center line and the boundaries on both sides is 10H in the spanwise direction. The height of the whole domain is about 11.1H. The coordinate origin locates at the nose tip of TC.

It is well known that as the train speed exceeds Mach 0.3, flow compressibility needs to be considered because of the large air density change (Tian, 2007). As the maglev train runs at 600 km/h in open and moderate air, the Mach number reaches about 0.5, leading to an obvious air compression effect. As for boundary conditions, the pressure inlet condition is usually applied on the boundary inlet of the compressible flow because of the density change. The total pressure of the inlet can be expressed by (Anderson, 2017)

$$P_0=P_s\left(1+\frac{1+\gamma}{2}M^2\right)^{\gamma/(\gamma-1)}, \tag{1}$$

where γ and P_s denote specific heat ratio and static pressure. Mach number M is defined as

$$M=\frac{V_{train}}{\sqrt{\gamma RT}}, \tag{2}$$

where V_{train}, R, and T denote the running speed, the specific gas constant, and the static temperature, respectively.

By calculation, the total and static pressures on the pressure inlet are hence about 120193 Pa and 101325 Pa, respectively. The static pressure on the pressure outlet equals standard atmospheric pressure. Symmetry planes on both sides of and above the train are regarded to be symmetrical. Both ground and track are non-slip moving walls at the same speed as the inflow to eliminate the boundary layer. The turbulent kinetic energy k and the specific dissipation rate ω on the pressure inlet can be used to describe the turbulent effect of the incoming flow on the maglev train. They are calculated by the following equations, respectively (ANSYS Inc., 2015):

$$k=\frac{3}{2}(I\cdot V_{train})^2, \tag{3}$$

$$\omega=\frac{\sqrt{k}}{0.07H\cdot C^{0.25}}, \tag{4}$$

where I and C are the turbulent intensity and empirical constant of 0.09, respectively.

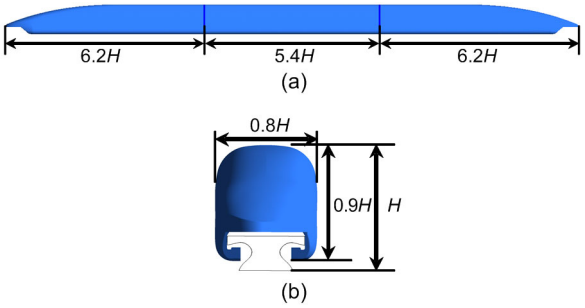

Fig. 1 Maglev train model
(a) Side view; (b) Front view

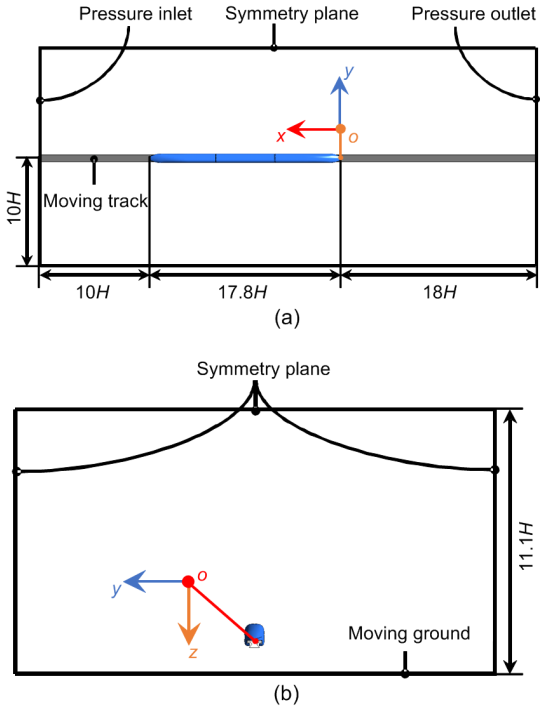

Fig. 2 Diagram of the computational domain layout
(a) Top view; (b) Front view

Generally, the inlet turbulent intensity reaches about 1% or less in the wind test (Wang et al., 2019). Compared with the wind test, the actual running may suffer from the environment with a larger turbulent intensity. Because of the lack of the turbulence

measurement data of the actual intensity, a turbulent intensity of 2% is used to simulate the turbulent effect.

2.3 Mesh generation

The numerical precision obtained by IDDES method is highly dependent on mesh quality and quantity. For one thing, considering the high ratio of the characteristic height to suspension gap and the complicated free-form surface of the train, hybrid meshes are used to fill the computational domain to ensure good mesh quality. For another, a different mesh quantity usually causes the differences of numerical results to some extent. In the area around the train and wake area which are full of vortices in various scales, the refined meshes are helpful in capturing the vortex structures. Therefore, it is necessary to refine the meshes of the area near the train appropriately.

The mesh refinement areas are mainly divided into three parts: area D1 in the far field, area D2 around the whole train, and area D3 near TC and the wake. The specific size of each refinement area constituted by the cuboid is shown in Fig. 3. The generation of different numbers of meshes can be realized by combining refinement areas. Generally, the mesh sizes of D1, D2, and D3 gradually decrease in order. In this study, two sequentially refined meshes (coarse and fine) are constructed based on different refinement strategies. The inflation layers adjacent to the train wall are applied to capture the flow features in the boundary layer. The mesh smoothing method is applied in the interfaces of D1 and D2 and between the outer inflation layer and the hybrid meshes. Fig. 4 gives the side view of the mesh distribution around the maglev train under the fine meshes. More numerical details regarding the mesh resolution are presented in Section 3.2.

2.4 Turbulence consideration

For the turbulence phenomena around the train, there is no doubt that direct numerical simulation (DNS) is the most accurate method to describe them. However, because of the complexity of train models, many turbulence solution methods such as unsteady Reynolds averaged Navier-Stokes (URANS), detached eddy simulation (DES), and large eddy simulation (LES) can be used to model the turbulence. Among them, the LES and URANS methods take the most and the least computation costs, respectively.

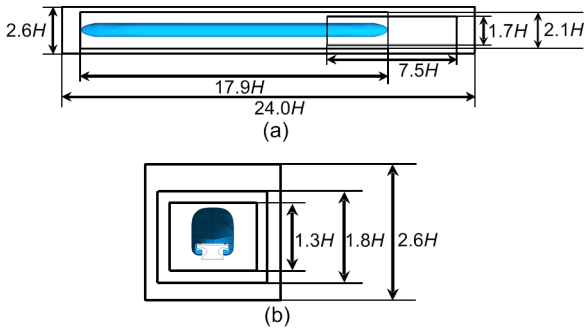

Fig. 3 Diagram of the refinement area distribution in the domain

(a) Top view; (b) Front view

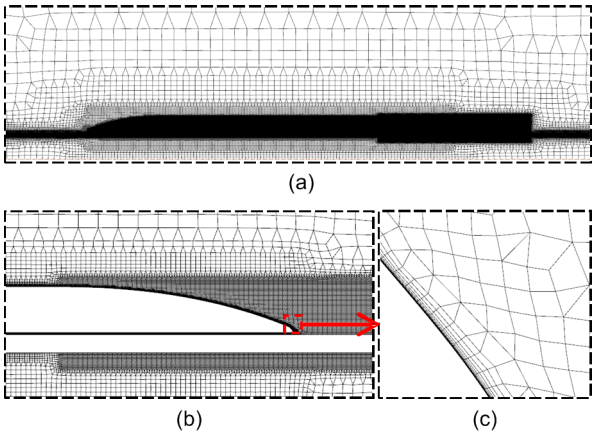

Fig. 4 Side view of the mesh distribution

(a) Near the whole train; (b) Near wake area; (c) Inflation layers

The LES method is mainly used for solving flow problems induced by the low-speed scaling train (Östh and Krajnović, 2012; Hemida et al., 2014), since there are still some difficulties in predicting the high Reynolds number flow. The URANS method cannot predict the cross-stream development of the trailing vortices well (Wang et al., 2017). However, the DES method combines the advantages of the URANS and LES methods, which means that the URANS method is used to deal with the small-scale vortex pulsation near the train wall, while the LES method is used to deal with the large-scale vortex development far away from the train wall, especially in the separation region. More importantly, the original DES method can easily suffer from the grid induced separation (GIS) problem, as the mesh spacing parallel to the wall becomes less than the boundary layer thickness (Spalart et al., 2006). Thus, the IDDES

method derived from delayed DES method, a hybrid RANS-LES, is established based on the modified sink term in the turbulence kinetic energy (k) equation of the shear stress transport (SST) model (Menter, 1994). In the URANS simulation for the area near the wall, the k transport equation can be written as

$$\frac{\partial \rho k}{\partial t}+\frac{\partial \rho \boldsymbol{u}_j k}{\partial \boldsymbol{x}_j}=\frac{\partial}{\partial \boldsymbol{x}_j}\left[\left(\mu+\frac{\mu_{\mathrm{t}}}{\sigma_k}\right)\frac{\partial k}{\partial \boldsymbol{x}_j}\right]+\boldsymbol{\tau}_{ij}\boldsymbol{S}_{ij}-\frac{\rho k^{1.5}}{l_{\mathrm{IDDES}}}, \quad (5)$$

where t, $\boldsymbol{u}_j$, $\boldsymbol{x}_j$, μ, μ_{t}, ρ, σ_k, $\boldsymbol{\tau}_{ij}$, and $\boldsymbol{S}_{ij}$ are the time, velocity vector, position vector, molecular viscosity, turbulent viscosity, density, turbulent Prandtl number for k, stress tensor, and mean strain rate tensor, respectively. The IDDES length scale l_{IDDES} can be defined as (Shur et al., 2008)

$$l_{\mathrm{IDDES}}=F_{\mathrm{d}}(1+f_{\mathrm{e}})\frac{\sqrt{k}}{\beta^{*}\omega}+(1-F_{\mathrm{d}})C_{\mathrm{DES}}\Delta, \quad (6)$$

where F_{d} and C_{DES} are the blending function and empirical constant of 0.65, respectively. f_{e} is larger than zero as the inflow has turbulent content; otherwise, it equals zero. β^{*} is the term defined by Menter (1994). The subgrid length scale Δ can be defined by

$$\Delta=\min(\max(C_{\mathrm{w}}d, C_{\mathrm{w}}h_{\max}, h_{\mathrm{wn}}), h_{\max}), \quad (7)$$

where C_{w}, d, $h_{\max}$, and h_{wn} are the empirical constant that is set to 0.15, the distance to the closest wall, the maximum edge length of the cell, and the wall-normal grid spacing, respectively.

More details about the F_{d} and f_{e} model can be found in the original reference (Shur et al., 2008).

2.5 Solver description

The numerical solutions can be realized by the implicit density-based solver of ANSYS Fluent 15.0 that solves the continuity, momentum, and energy equations simultaneously and turbulence and other scalar equations later. The Roe flux-difference splitting method is used to calculate convective fluxes. For spatial discretization, the least squares method is used to evaluate the gradients. This is proper for irregular unstructured meshes. The second-order upwind scheme is used to discretize flow and turbulence terms. For the time-accurate calculations, the dual-time formulation is adopted. The time-dependent physical term is discretized in an implicit method by the second-order Euler backwards. The implicit pseudo-time marching method is used to carry out a series of inner iterations. For convenience of the Fourier change made on the related time-domain data, the constant simulation time step is selected to guarantee a fixed sample interval. In the whole transient simulation, the time step is 0.0002 s, which can fully capture quasi-periodic change of the flow field.

In order to shorten the computational time for the flow field around the maglev train to reach quasi-periodic fluctuation, the converged-state steady results based on the k-ω model are obtained first. Then, those steady results are taken as the initial conditions of the unsteady solution process under the IDDES method. As the simulation time is about 1 s, the flow field structure around the maglev train reaches a relative equilibrium state that the relevant physical quantities fluctuate with time in a quasi-periodic manner. At this time, the time-averaged method is applied to handle the flow field solution so as to get the statistical data of the flow field. As the simulation continues for about 2.2 s, the transient solution process ends. The whole transient simulation process lasts for 3.2 s, about 2.5 times the time taken for the freestream flow to pass through the distance of a computational domain length in the streamwise direction, or about 6.5 times the time taken for the freestream flow to pass through the distance of the maglev train length.

2.6 Data processing method

To facilitate the analyses of numerical results, some commonly used aerodynamic coefficients can be defined as follows (Tian, 2007):

$$C_i=\frac{F_i}{0.5\rho_\infty U_\infty^2 A}, \quad (8)$$

$$C_{\mathrm{p}}=\frac{P-P_\infty}{0.5\rho_\infty U_\infty^2}, \quad (9)$$

where C_i, C_{p}, F_i, A, ρ_∞, U_∞, P, and P_∞ are the aerodynamic force coefficient in the i direction, the pressure coefficient, the force in the i direction, the cross-sectional area of the train, and the density, velocity, local surface pressure, and static pressure of the far incoming flow, respectively.

In the study of the high-speed train's slipstream, only its component in the horizontal plane is considered, that is, the vertical component is often ignored (Wang et al., 2018). Given the large vertical component of the slipstream caused by the high-speed maglev train, the magnitude of the slipstream velocity can be defined as

$$V_{\text{slip}}=\sqrt{U_{\text{GF}}^2+V_{\text{GF}}^2+W_{\text{GF}}^2}, \tag{10}$$

where U_{GF}, V_{GF}, and W_{GF} are the streamwise component, spanwise component, and vertical component of the slipstream velocity, respectively, based on a ground-fixed coordinate system. U_{GF}, V_{GF}, and W_{GF} are defined by

$$U_{\text{GF}}=\frac{U_\infty-U_{\text{TF}}}{U_\infty}, \tag{11}$$

$$V_{\text{GF}}=\frac{V_{\text{TF}}}{U_\infty}, \tag{12}$$

$$W_{\text{GF}}=\frac{W_{\text{TF}}}{U_\infty}, \tag{13}$$

where U_{TF}, V_{TF}, and W_{TF} are the streamwise component, spanwise component, and vertical component of the slipstream velocity, respectively, based on a train-fixed coordinate system.

In order to describe the local balance between shear strain rate and vorticity magnitude, the second invariant Q is defined by (Hunt et al., 1988)

$$Q=\frac{1}{2}(\|\boldsymbol{\Omega}\|-\|\boldsymbol{S}\|), \tag{14}$$

where $\boldsymbol{S}$ and $\boldsymbol{\Omega}$ are the symmetric and anti-symmetric parts of the velocity gradient tensor, respectively.

For the transient flow induced by the maglev train, the flow state changes with time. However, sometimes the statistical characteristics of the flow are more concerned in the whole simulation. The time-averaged data of a particular physical index can be defined by

$$\overline{q}_i=\sum_{i=m}^{n}\frac{q_i}{i+1-m}, \tag{15}$$

where q_i, i, m, and n represent the transient value of any physical index, the ith time step, start time step, and end time step, respectively. In the study, the physical index with top bar is regarded as the time-averaged variable.

In addition, the dimensionless time t^* can be defined as

$$t^*=\frac{tV_{\text{train}}}{H}. \tag{16}$$

3 Results and discussion

3.1 Numerical verification

In order to verify the reliability of the numerical method for simulating the compressible flow caused by the high-speed maglev train, the TR08 maglev train is taken as the study object. For the new maglev train, the main dimensions of the TR08 train such as height and width are almost the same, except for the shorter streamline length of about 5 m. The experimental method and data acquisition related to the TR08 maglev train running on the Shanghai maglev test line have been reported in previous studies (Bi et al., 2005; Li et al., 2006). To compare the difference between the test results and the numerical results, two monitoring sensors P_1 and P_2 are placed 8.6 m and 14.9 m away from the TC nose tip, respectively, as shown in Fig. 5a. The entire computational domain

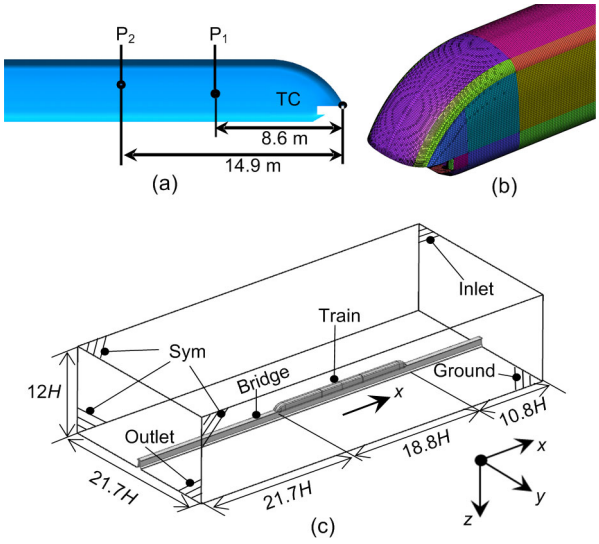

Fig. 5 Numerical configuration of the TR08 maglev train
(a) Monitoring position; (b) Surface mesh distribution; (c) Domain and boundary conditions

filled with about 32 million Cartesian/prism meshes keeps the same dimensions and boundary condition types as those in Section 2.2, as shown in Fig. 5c. As the TR08 maglev train runs at 430 km/h on the 5 m-high bridge, the total pressure at inlet is about 109971.2 Pa based on Eq. (1). Table 1 gives the time-averaged pressure coefficients at P_1 and P_2 obtained by the numerical simulation or experiment. It can be seen that the relative errors between the simulation and the experimental values of the pressure coefficients at P_1 and P_2 are about 6.6% and 6.5%, respectively, which shows the feasibility of the numerical method in this study.

Table 1 Comparison of the time-average pressure coefficients between experiment and numerical simulation

Method	Time-average pressure coefficient	
	P_1	P_2
Experiment	0.034	0.016
Simulation	0.032	0.015
Relative error	6.6%	6.5%

3.2 Mesh resolution influence

Based on the mesh generation strategy described in Section 2.3 the two sets of meshes consisting of about 42 million and 50 million cells, respectively, are used to study the influence of mesh resolution on the numerical results. The maximum surface mesh sizes of the train under coarse and fine meshes are about 80 mm and 40 mm, respectively. Both sets of meshes have the same inflation layer distribution laws that 18 inflation layers with the growth rate of 1.2 are split and the normal distance between the first layer meshes and the train wall is 0.01 mm. Fig. 6 shows the slipstream monitoring lattice on the right side of the running direction and naming rules of the monitoring position. The spacing distances of the monitoring line in the spanwise direction and vertical direction are L and $2L$, respectively, and L=0.5 m. The spanwise and vertical distances of l_{11} from the center of track (COT) and top of track (TOT) are $5L$ and $2L$, respectively.

Fig. 7 shows the differences of the numerical results under coarse and fine meshes. On the whole, the mesh resolution has little influence on the drag coefficient, but has great influence on the lift coefficient. By further comparison, the drag coefficient error and lift coefficient error are of the order of 0.04% and 0.8%, meaning that the drag and lift errors are about less than 100 N and 2000 N, respectively. The drag and lift of the maglev train are determined by the viscous and pressure forces that are sensitive to the boundary layer mesh distribution and the train surface mesh distribution, respectively. Since the inflation layers under the two sets of meshes are almost the same, the drag error generated by pressure difference between them is not large. However, the maximum mesh size of the train surface under fine mesh is half of that under coarse mesh, which leads to the large change of lift. Generally speaking, the lift force can be accurately predicted when the mesh size of the train surface is fine enough. Therefore, the subsequent results are discussed based on the fine meshes.

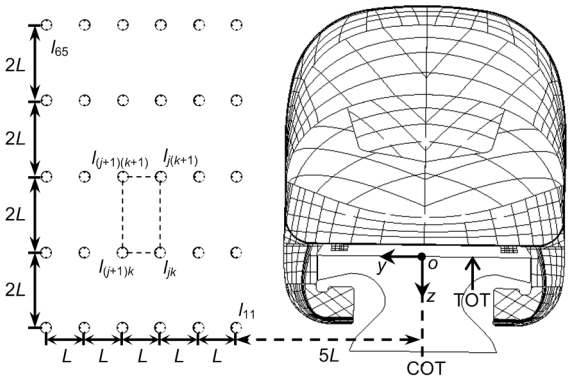

Fig. 6 Front view of the slipstream monitoring location

3.3 Aerodynamic loads

The comparisons between the instantaneous and time-averaged aerodynamic coefficients are given in Figs. 8a and 8b. Clearly, the instantaneous drag coefficient and lift coefficient have quasi-periodic fluctuations with time, but their time-averaged values gradually tend to be steady. The negative pressure mainly occurs in the upper non-streamlined part of the train and the bottom of HC nose and skirt plate, as shown in Fig. 8c. Most areas on the suspension floor suffer from the positive pressure against the train gravity. Meantime, the positive pressure value on the suspension floor increases gradually along the opposite direction of the train motion, so that the lift of TC is larger than that of HC or MC. Near the nose tip of TC, local positive pressure contributes to reducing the aerodynamic drag of TC.

In addition, the aerodynamic coefficients show obvious unsteady features caused by the unsteady development of the vortices around the maglev train. Fig. 9 shows the normalized amplitude changes of aerodynamic coefficients for each car by the fast Fourier transform (FFT) method (Duhamel and Vetterli, 1990). On the whole, the aerodynamic coefficients of each car show obvious low-frequency information and have the scattered main frequency. The main frequencies corresponding to the maximum drag amplitudes of HC, MC, and TC are about 0.6 Hz, 17.1 Hz, and 25.9 Hz, respectively. MC has an obvious secondary frequency of about 68.0 Hz. Similar to the MC drag, the lift has an obvious secondary frequency approaching the main frequency of TC lift. Overall, the main or secondary frequency of lift for each car is mainly within the range of 17 Hz to 28 Hz except for the main frequency of MC drag that is about 0.6 Hz.

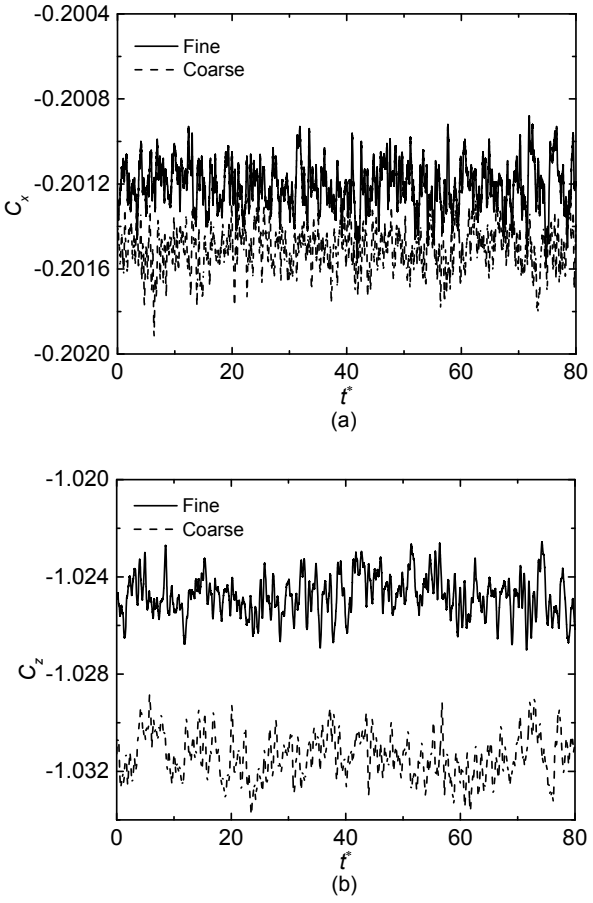

Fig. 7 Comparisons of the numerical results under different mesh quantities

(a) Drag coefficient; (b) Lift coefficient

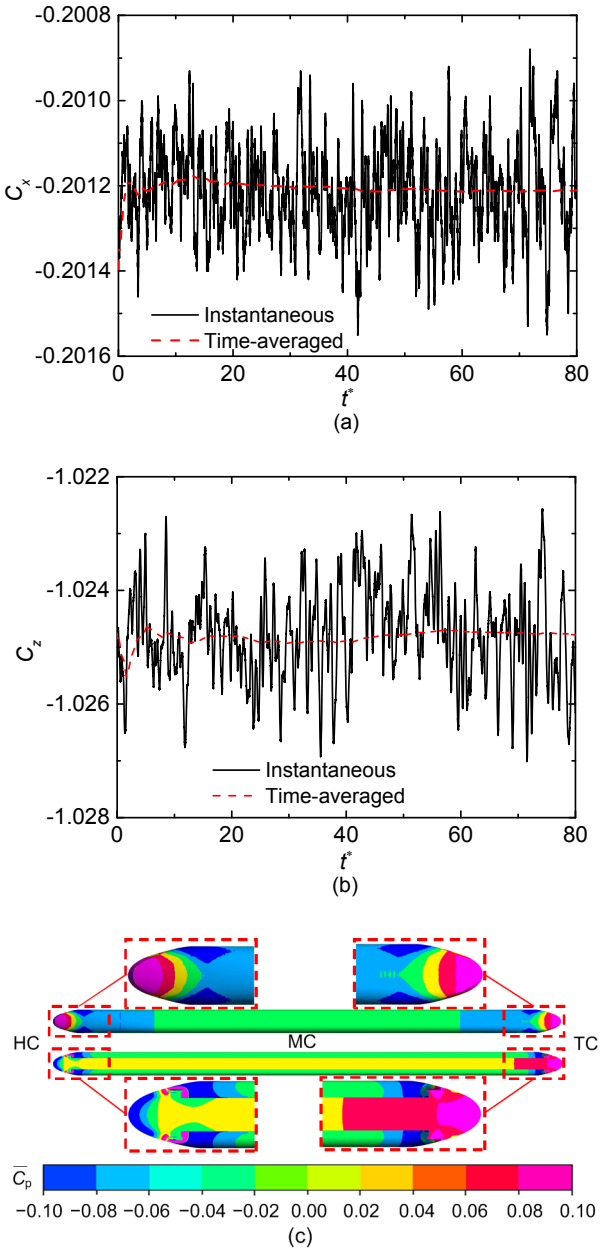

Fig. 8 Time-averaged load distribution of the maglev train

(a) Drag coefficient; (b) Lift coefficient; (c) Pressure coefficient of the maglev train surface

3.4 Boundary layer development

Fig. 10 shows the time-averaged boundary layer distribution around the maglev train. The time-averaged thickness of the boundary layer from HC to MC gradually increases in areas S_1, S_3, and S_5, from the front view, while the track bottom has no boundary layer in area S_4 due to its slip effect, as shown in

Fig. 10a. The time-averaged thickness of the boundary layer for each car reaches a maximum in areas S_2 and S_6, implying that the large vortex may be shed from the train wall. As the airflow passes by the MC end, the time-averaged thickness of the boundary layer reaches stability in areas S_1, S_3, and S_5. From the side view, the time-averaged thickness of the boundary layer in area A is almost unchanged, as shown in Fig. 10b. Area B is a low-pressure area formed because of expansion wave effect caused by the decrease of the train cross-sectional area. The airflow velocity gradient is therefore increased in area B, which makes the boundary layer thinner. However, the boundary layer is thicker in area C because of, to some extent, the reverse pressure gradient increase. In area D, the boundary layer is completely separated from the train surface and loses its physical meaning. Many vortices formed after separation mainly develop in the area within the velocity of $0.99U_\infty$.

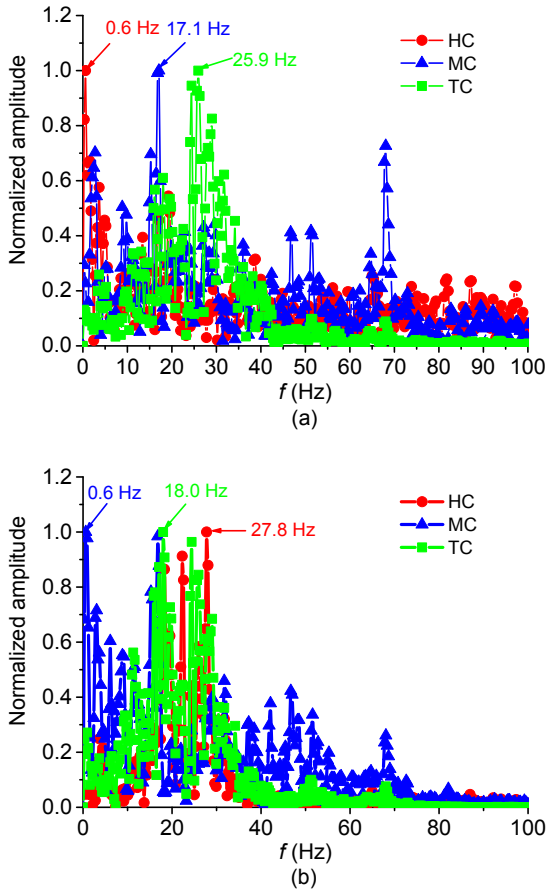

Fig. 9 Normalized amplitude changes of aerodynamic coefficients with frequency
(a) Drag coefficient; (b) Lift coefficient

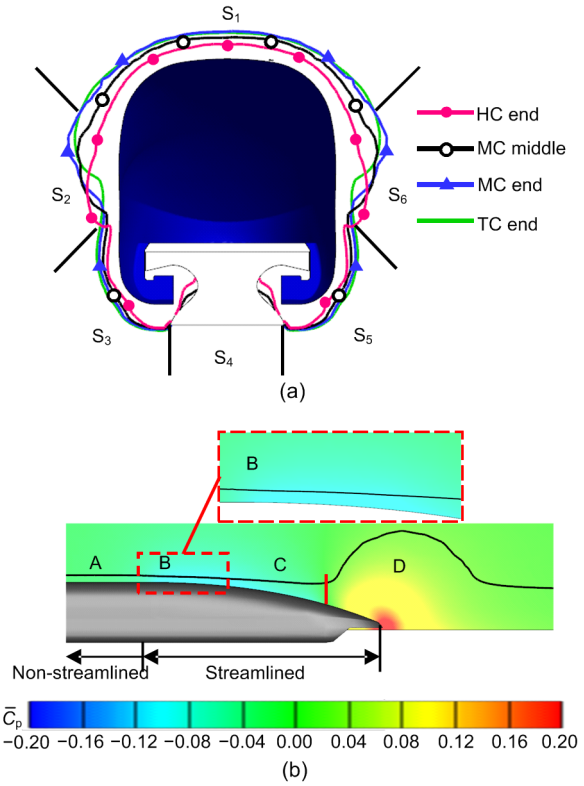

Fig. 10 Time-averaged boundary layer distribution on each car
(a) Front view; (b) Side view near TC

3.5 Vortex developments

3.5.1 Time-averaged vorticity distribution

With the high-speed movement, many vortices are inevitably generated around the maglev train, especially TC, due to the complex geometric curvature. The time-averaged vorticity distributions near TC at different heights are shown in Fig. 11. Typically, the monitoring surface slices through the suspension gap between track and skirt plates and the gap between track and train floor as z equals $0.04H$ and $-0.02H$, respectively. Because of the small clearance and fast airflow velocity, the two gaps are filled with many intensive vortices, as shown in Figs. 11b and 11c. In addition, the high-strength vortices are also distributed near the surface of the train or track. In the area near TOT, the influence range of the high-strength vorticity increases in both spanwise and streamwise directions gradually, as shown in Figs. 11c and 11d. With the increase of the height from TOT, the vorticity in the wake decreases clearly, as shown in Fig. 11e. The time-averaged vorticity distribution of

the wake has approximate symmetry under different heights except z=−0.02H.

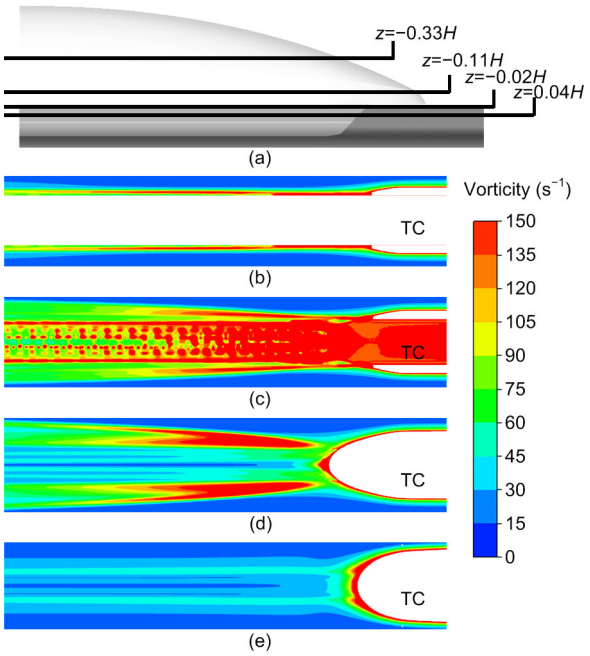

Fig. 11 Time-averaged vorticity distributions near TC at different heights

(a) Monitoring section position; (b) z=0.04H; (c) z=−0.02H; (d) z=−0.11H; (e) z=−0.33H

3.5.2 Streamwise vortex structures near the train

Fig. 12 shows the time-averaged velocity streamline distributions under some typical cross-sections colored by the time-averaged streamwise vorticity component ω_x. The cross-section slices through the non-streamlined middle parts of HC, MC, and TC as x is 13H, 8.9H, and 4.8H, respectively. In the non-streamlined part of the train, a counter-rotating large vortex pair such as A, C, or E falling off the train shoulder occurs on the both sides of the train. Another counter-rotating large vortex pair such as B, D, or F shedding from the high curvature part of track occurs on the lower left and right corners of the track. These large vortex pairs thicken the train boundary layer as shown in Fig. 10. Along the streamwise direction, the large vortices tend to be away from the train or track wall. Near the nose tip of TC, a large vortex pair G is close to TOT, accompanied by some small vortices. In addition, the large vortex pair K appears near the track with the large curvature, as shown in Fig. 12d. Because there is no restraint exerted by the train skirt plates, vortex pair K cannot fall off both sides of the track as quickly as B, D, and F. The cores of the large vortex pair G move to both sides of the track and reproduce the relatively small

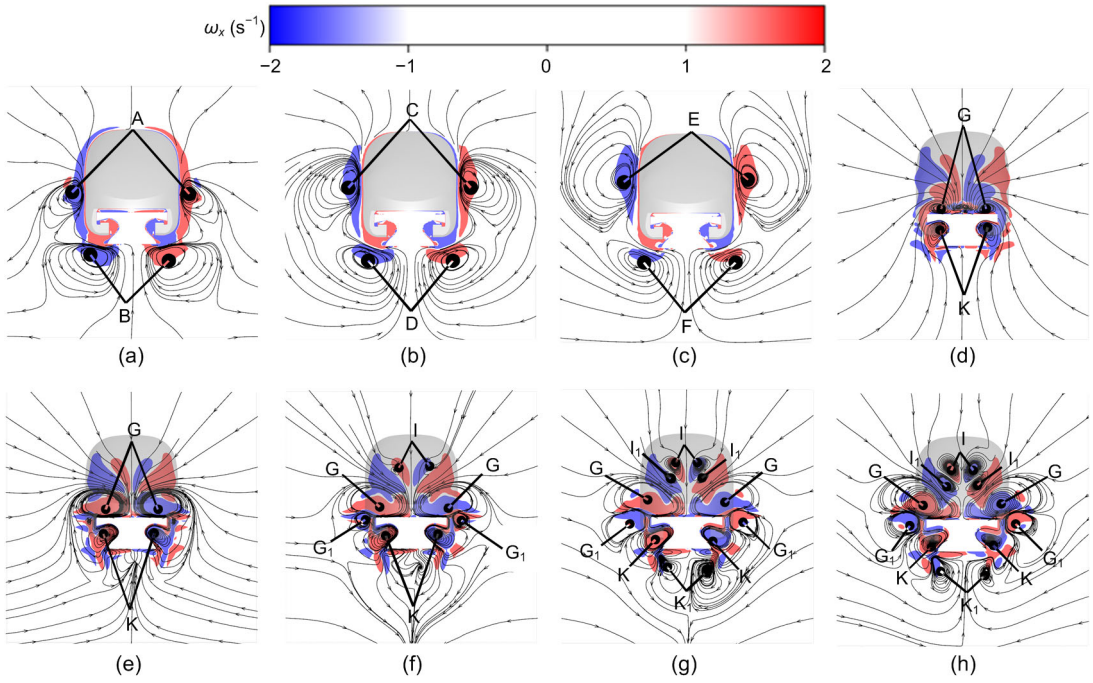

Fig. 12 Time-averaged streamlines under different cross-sections along with vorticity distributions

(a) x=13H; (b) x=8.9H; (c) x=4.8H; (d) x=0H; (e) x=−1H; (f) x=−2H; (g) x=−3H; (h) x=−4H

vortex pair G_1 near the track corner, expanding its influence ranges further, as shown in Fig. 12f. Similar to the large vortex pair G, the large vortex pair K and the small vortex pair I undergo the process of expanding and multiplying along the streamwise direction, as shown in Figs. 12g and 12h. Compared with the large vortex pairs, all the small vortex pairs move downward for a certain distance. Along with the formations of the small vortex pairs, the distribution range of the streamwise vorticity expands.

To show the vortex distribution in the wake more vividly, the 3D vortex core distribution colored by the vorticity is given in Fig. 13. The large vortex pairs G and K develop in the streamwise direction in a spiral way and expand slightly in the spanwise and vertical directions. The ribbon vortex pair J falling off the nose tip of TC decays gradually along the streamwise direction. Along with the expansion and propagation of large vortices downstream, the vorticity has a decreasing trend due to the air viscosity. The wake is full of vortices of different sizes and intensities leading to quite a complicated wake.

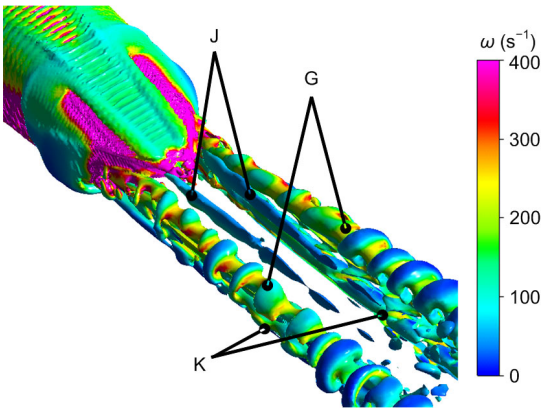

Fig. 13 Vortex core distribution in wake as t^*=80 (Q=70)

3.5.3 Frequency-domain characteristics

Based on the above analyses, the high-strength vorticity is mainly distributed in the suspension gap and wake area. Fig. 14 shows the monitoring point cloud distribution. Among them, 20 monitoring points with the interval of 8L are set between the train floor and TOT and two layers of monitoring points including 30 monitoring points are put above TOT. The first and second layers of monitoring points are L and 3L from TOT, respectively. P_i represents the ith point in the middle of the gap and i increases sequentially in the $-x$ direction. For example, the streamwise distance between P_1 and the nose tip of HC is 4.6L. $P_{wi\text{-}j}$ represents the jth point in the ith vertical plane in wake. As for the index, i increases sequentially in the $-x$ direction and j increases sequentially in the $+y$ and $-z$ directions. For example, the streamwise, spanwise, and vertical distances of $P_{w1\text{-}1}$ from the nose tip of TC, TOC, and TOT are H, 2L, and L, respectively.

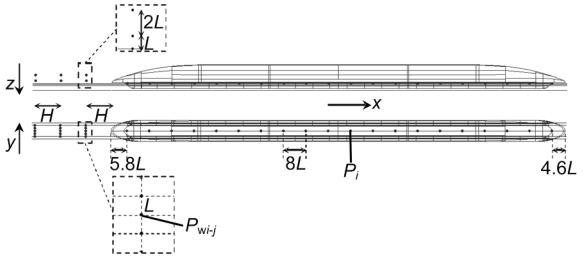

Fig. 14 Schematic diagram of the monitoring point position

Fig. 15 shows the frequency-domain characteristics of the pressure coefficients at different monitoring positions in the gap. All the monitoring points except for P_{20} close to the TC nose have the same main frequencies of about 27.8 Hz, indicating that the vortex-shedding frequency has little change in the streamwise direction. P_{20} is not bound by skirt plates on both sides and its main frequency and amplitude increase simultaneously because of the complicated wake. In addition, the amplitude of pressure coefficient increases a little in the streamwise direction indicating that vorticity increases in the streamwise direction. In order to quantitatively discuss the "increase" trend, 19 monitoring points except for P_{20} are here selected at the same main frequency. In space, the pressure coefficient amplitude increases exponentially in the streamwise direction as shown in Fig. 16. Due to the turbulence effect, the maximum amplitude and main frequency of pressure coefficient in the wake have quite complex, irregular, and random distribution characteristics as shown in Table 2. In the same cross-section, the main frequency and corresponding amplitude of the symmetrical monitoring points, such as ($P_{w1\text{-}1}$, $P_{w1\text{-}5}$) and ($P_{w2\text{-}6}$, $P_{w2\text{-}10}$), may be different. On the same horizontal plane, the main frequency and corresponding amplitude do not decrease monotonically in the streamwise direction. For the streamwise monitoring points such as ($P_{w1\text{-}1}$,

$P_{w2\text{-}1}$, $P_{w3\text{-}1}$) and ($P_{w1\text{-}9}$, $P_{w2\text{-}9}$, $P_{w3\text{-}9}$), even if the maximum amplitude changes, the corresponding main frequency remains the same. For the vertical monitoring points such as ($P_{w2\text{-}5}$, $P_{w2\text{-}10}$) and ($P_{w3\text{-}5}$, $P_{w3\text{-}10}$), the main frequency and corresponding amplitude keep constant as the height increases.

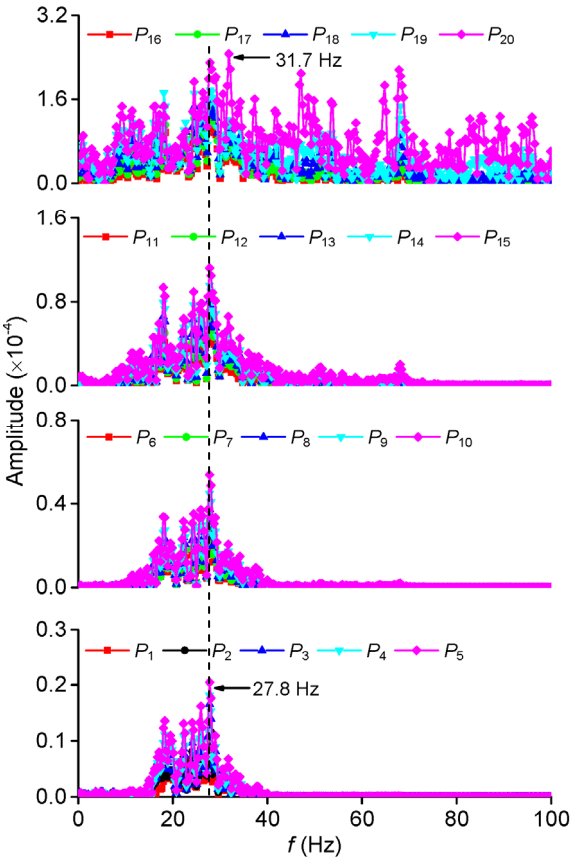

Fig. 15 Variation of pressure coefficient amplitude to frequency for different monitoring positions in the gap

3.6 Time-averaged slipstream velocity

Like the high-speed train, the high-speed movement of the maglev train is accompanied by the generation of a slipstream, which may cause safety problems for people near the train. The slipstream monitoring location has been illustrated in Fig. 6 and the corresponding time-averaged slipstream velocity normalized by the train speed (V_{slip}/V_{train}) is given in Fig. 17. It is easy to find that the farther away from the train, the lower peak value of time-averaged velocity. The variation of the time-averaged velocity in the streamwise direction can be divided into five main processes. Based on the ground-fixed coordinate system, in the first process A, the time-averaged velocity is almost zero due to little disturbance generated by the train. In process B, as the slipstream passes by the HC nose ($x\approx17H$), the time-averaged velocity increases to the maximum value due to the intense shock by HC

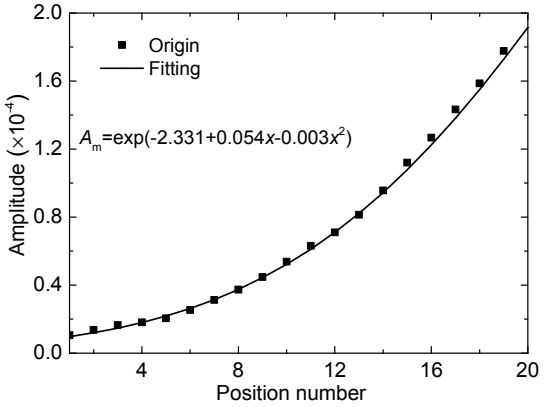

Fig. 16 Change of the pressure coefficient amplitude (A_m) with the monitoring point position

Table 2 The maximum amplitude and main frequency of pressure coefficient at different positions in wake

z plane	Position (x=1H)	Amplitude ($\times10^{-4}$)	Main frequency (Hz)	Position (x=2H)	Amplitude ($\times10^{-4}$)	Main frequency (Hz)	Position (x=3H)	Amplitude ($\times10^{-4}$)	Main frequency (Hz)
	$P_{w1\text{-}1}$	9.63	68.0	$P_{w2\text{-}1}$	8.10	68.0	$P_{w3\text{-}1}$	9.55	68.0
	$P_{w1\text{-}2}$	1.14	68.0	$P_{w2\text{-}2}$	1.08	48.5	$P_{w3\text{-}2}$	1.14	48.5
z=1L	$P_{w1\text{-}3}$	0.56	16.8	$P_{w2\text{-}3}$	0.39	40.0	$P_{w3\text{-}3}$	0.63	58.9
	$P_{w1\text{-}4}$	1.07	16.8	$P_{w2\text{-}4}$	0.83	57.1	$P_{w3\text{-}4}$	0.84	58.9
	$P_{w1\text{-}5}$	0.60	16.8	$P_{w2\text{-}5}$	0.43	16.8	$P_{w3\text{-}5}$	0.61	60.1
	$P_{w1\text{-}6}$	0.58	16.8	$P_{w2\text{-}6}$	0.39	26.3	$P_{w3\text{-}6}$	0.60	67.1
	$P_{w1\text{-}7}$	0.48	16.8	$P_{w2\text{-}7}$	0.24	40.0	$P_{w3\text{-}7}$	0.34	16.8
z=3L	$P_{w1\text{-}8}$	0.47	16.8	$P_{w2\text{-}8}$	0.24	16.8	$P_{w3\text{-}8}$	0.30	16.8
	$P_{w1\text{-}9}$	0.48	16.8	$P_{w2\text{-}9}$	0.27	16.8	$P_{w3\text{-}9}$	0.29	16.8
	$P_{w1\text{-}10}$	0.60	16.8	$P_{w2\text{-}10}$	0.43	16.8	$P_{w3\text{-}10}$	0.61	60.1

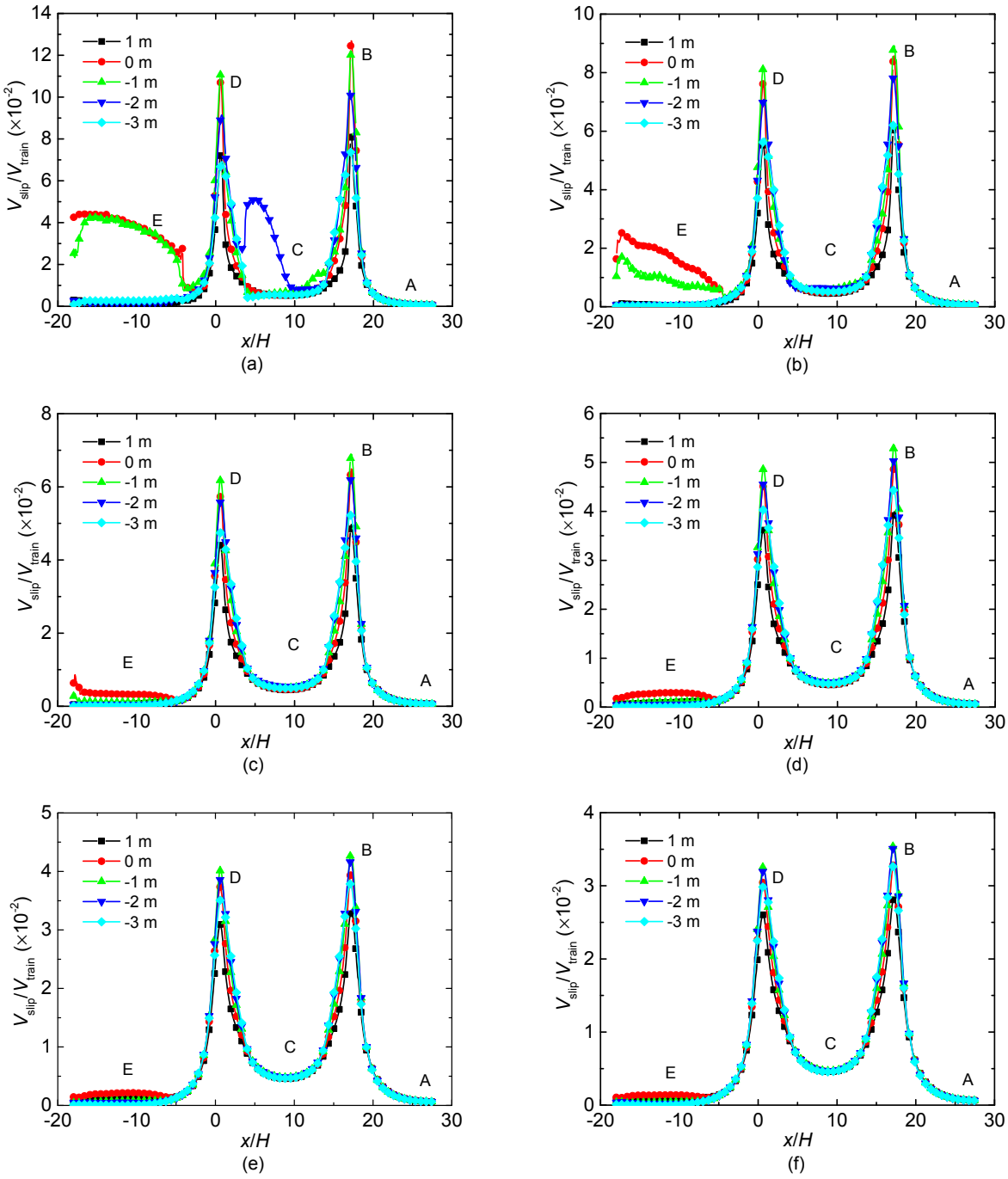

Fig. 17 Time-averaged slipstream velocity distributions at different spanwise distances from COT
(a) x=5L; (b) x=6L; (c) x=7L; (d) x=8L; (e) x=9L; (f) x=10L

and decreases to steady value later with compressive shock weakened. In process C, the slipstream mainly goes by MC and non-streamlined part of TC. Except for the position of −2 m from TOT and 5L from COT in Fig. 17a, the slipstream in other monitoring positions reaches the steady state with a small time-averaged velocity. The duration of this steady state mainly depends on the non-streamlined length of the train and spanwise distance from COT. The streamwise steady range in this steady state narrows with the increasing distance from COT. In process D, the slipstream mainly goes by the TC streamlined part

and experiences another pulse change of the time-averaged velocity. The time-averaged velocity increases and decreases rapidly due to the low pressure in the wake, and its peak value is a little lower than the first peak value. In process E, the slipstream mainly goes by the wake area. In the position of 0 m or −1 m from TOT in Figs. 17a and 17b, the time-averaged velocity increases in the form of small fluctuations along with the unsteady development of vortices. Nevertheless, the time-averaged slipstream velocity decreases gradually in other monitoring positions until it reaches the steady state as the slipstream moves away from the wake area.

The maximum slipstream velocity is the most critical parameter for dividing the track-side safe domain. In China this is regarded to be acceptable if it is less than 14 m/s (Tian, 2007). According to Fig. 17, for the certain distance from COT, the maximum time-averaged slipstream velocity may appear at −1 m or 0 m from TOT. In order to determine more accurately the height at which the maximum slipstream velocity occurs, based on the intersection of the cross-section (x=17H) and longitudinal section (y=2.5 m), the vertical slipstream velocity distribution is shown in Fig. 18a. The maximum time-averaged velocity occurs 0.17H above TOT. Based on the intersection of the cross-section (x=17H) and horizontal section (z=−0.17H), the streamwise velocity is plotted and the track-side safe domain can be further determined, as shown in Fig. 18b. The track-side person stationed in the domain with 0.69H (about 3.14 m) distance from COT is regarded to be extremely unsafe.

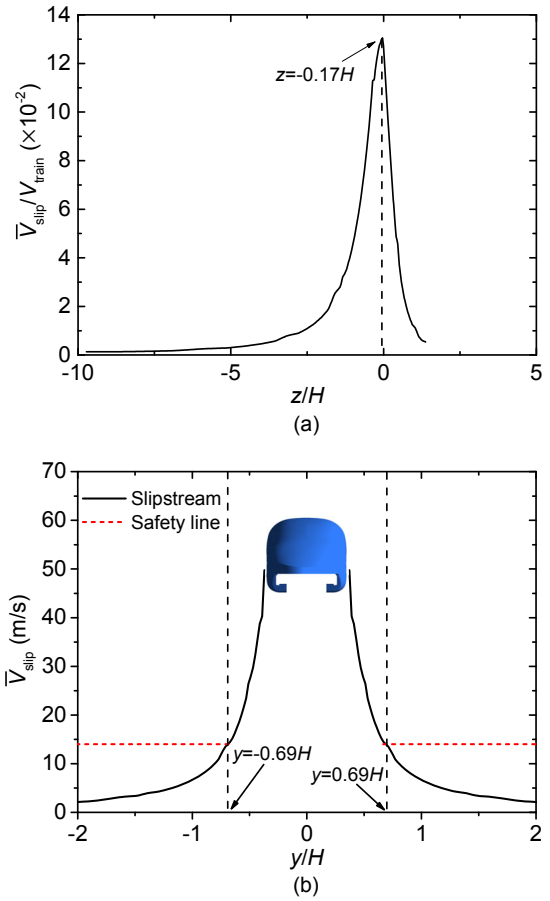

Fig. 18 Slipstream velocity distributions in the vertical direction (a) and track-side safety area (b)

4 Conclusions

In this study, the basic aerodynamic characteristics of a new maglev train running at 600 km/h are studied. The study clarifies some variation characteristics of the aerodynamic loads, vortex developments, and slipstreams of the maglev train, and lays the foundation for deep running safety analyses in the future. The main conclusions drawn from the numerical results are:

1. The new maglev has the following aerodynamic load performance: the proper positive pressure distribution on the train floor that contributes to the train suspension and energy conservation, positive pressure distribution near TC nose that contributes to small drag coefficient, dispersed main frequency of the aerodynamic force for each car, etc.

2. The large vortex shedding from the wall surface may break an obvious rule of wall boundary layer development that its thickness gradually increases in the streamwise direction. For example, the boundary layer thickness of a particular position of the HC may be smaller or larger than that of the same part of the TC. The development of the boundary layer at the top of TC is relatively complex because of the adverse pressure gradient, expansion wave, etc.

3. Many high-intensity vortices are distributed in the narrow space between skirt plates or train floor and track. In the non-streamlined part of the maglev train, there are two pairs of counter-rotating large vortices close to the train or track surface. These originate from the train shoulder and high curvature

part of the track. In the wake, there are two pairs of counter-rotating spiral vortices and a pair of ribbon vortices. The counter-rotating vortices gradually expand and produce descendants that move downward for a certain distance. In the gap between the train floor and track top (except near the TC nose), the vorticity increases exponentially in the streamwise direction, while the corresponding main frequency remains unchanged. In the wake, the vortex has quite complex, irregular, and random distribution characteristics due to turbulence.

4. The time-averaged slipstream development of the maglev train can be mainly divided into five typical processes. Because of the shock generated by the HC nose, the time-averaged slipstream velocity near it suddenly increases and reaches the maximum value. Because of the low-pressure area, the time-averaged slipstream velocity near the TC nose suddenly increases with smaller amplitudes than that near the HC nose. In order to ensure the safety of the track-side person, it should be at least 3.14 m away from the track center line.

Acknowledgements

CRRC Qiangdao Sifang, China is gratefully acknowledged for providing the geometric model of maglev train. Besides, the authors acknowledge the Supercomputing Center in National Laboratory of Rail Transportation (Building) of China for providing the computational resources.

Contributors

Tian LI guided the turbulence modeling approach. Chun-fa ZHAO and Ji-ye ZHANG provided the critical computing resources and guided the research process. Peng ZHOU designed the research method, completed the numerical simulation, carried out the relevant data analysis, and wrote and modified the paper.

Conflict of interest

Peng ZHOU, Tian LI, Chun-fa ZHAO, and Ji-ye ZHANG declare that they have no conflict of interest.

References

Anderson JD, 2017. Fundamentals of Aerodynamics, 6th Edition. McGraw-Hill Education, New York, USA, p.530-550.

ANSYS Inc., 2015. ANSYS Fluent Theory Guide. ANSYS Inc., Canonsburg, USA.

Bi HQ, Lei B, Zhang WH, 2004. Research on numerical calculation for aerodynamic characteristics of the TR maglev train. *Journal of the China Railway Society*, 26(4):51-54 (in Chinese). https://doi.org/10.3321/j.issn:1001-8360.2004.04.011

Bi HQ, Lei B, Zhang WH, 2005. Numerical calculation for turbulent flow around TR maglev train. *Journal of Southwest Jiaotong University*, 40(1):5-8 (in Chinese). https://doi.org/10.3969/j.issn.0258-2724.2005.01.002

Chen JX, 2018. Study on Crossing Air Pressure Pulse and Aerodynamic Performance of High-speed Maglev Trains Meeting in the Open Air. MS Thesis, Lanzhou Jiaotong University, Lanzhou, China (in Chinese).

Deng ZG, Zhang Y, Wang B, et al., 2019. Present situation and prospect of evacuated tube transportation system. *Journal of Southwest Jiaotong University*, 54(5):1063-1072 (in Chinese). https://doi.org/10.3969/j.issn.0258-2724.20180204

Duhamel P, Vetterli M, 1990. Fast Fourier transforms: a tutorial review and a state of the art. *Signal Processing*, 19(4):259-299. https://doi.org/10.1016/0165-1684(90)90158-U

Hemida H, Baker C, Gao GJ, 2014. The calculation of train slipstreams using large-eddy simulation. *Proceedings of the Institution of Mechanical Engineers, Part F: Journal of Rail and Rapid Transit*, 228(1):25-36. https://doi.org/10.1177/0954409712460982

Huang S, Li ZW, Yang MZ, 2019. Aerodynamics of high-speed maglev trains passing each other in open air. *Journal of Wind Engineering and Industrial Aerodynamics*, 188:151-160. https://doi.org/10.1016/j.jweia.2019.02.025

Hunt JCR, Wray AA, Moin P, 1988. Eddies, stream, and convergence zones in turbulent flows. Proceeding of the Summer Program in Center for Turbulence Research, p.193-208.

Jia YX, Mei YG, 2018. Numerical simulation of pressure waves induced by high-speed maglev trains passing through tunnels. *International Journal of Heat and Technology*, 36(2):687-696. https://doi.org/10.18280/ijht.360234

Lee HW, Kim KC, Lee J, 2006. Review of maglev train technologies. *IEEE Transactions on Magnetics*, 42(7): 1917-1925. https://doi.org/10.1109/TMAG.2006.875842

Lee J, Jo J, Han Y, et al., 2014. The development and application of guideway monitoring vehicle for super speed maglev. Proceedings of the 14th International Conference on Control, Automation and Systems, p.427-429. https://doi.org/10.1109/ICCAS.2014.6988036

Li MS, Lei B, Lin GB, et al., 2006. Field measurement of passing pressure and train induced airflow speed on high speed maglev vehicles. *Acta Aerodynamica Sinica*, 24(2): 209-212 (in Chinese). https://doi.org/10.3969/j.issn.0258-1825.2006.02.013

Li RX, Liu YQ, Zhai WM, 2004. Numerical analysis of aerodynamic force in longitudinal and vertical direction for high-speed maglev train. *China Railway Science*, 25(1): 8-12 (in Chinese). https://doi.org/10.3321/j.issn:1001-4632.2004.01.002

Li XB, Chen G, Wang Z, et al., 2019. Dynamic analysis of the flow fields around single- and double-unit trains. *Journal of Wind Engineering and Industrial Aerodynamics*, 188: 136-150. https://doi.org/10.1016/j.jweia.2019.02.015

Liu TH, Tian HQ, Wang CY, 2006. Aerodynamic performance comparison of several kind of nose shapes of maglev train. *Journal of National University of Defense Technology*, 28(3):94-98 (in Chinese). https://doi.org/10.3969/j.issn.1001-2486.2006.03.020

Menter FR, 1994. Two-equation eddy-viscosity turbulence models for engineering applications. *AIAA Journal*, 32(8): 1598-1605. https://doi.org/10.2514/3.12149

Miao BR, Zhang WH, Chi MR, et al., 2019. Analysis and prospects of key technical features of next generation high speed trains. *Journal of the China Railway Society*, 41(3):58-70 (in Chinese). https://doi.org/10.3969/j.issn.1001-8360.2019.03.008

Ono M, Koga S, Ohtsuki H, 2002. Japan's superconducting maglev train. *IEEE Instrumentation & Measurement Magazine*, 5(1):9-15. https://doi.org/10.1109/5289.988732

Östh J, Krajnović S, 2012. The flow around a simplified tractor-trailer model studied by large eddy simulation. *Journal of Wind Engineering and Industrial Aerodynamics*, 102:36-47. https://doi.org/10.1016/j.jweia.2011.12.007

Shur ML, Spalart PR, Strelets MK, et al., 2008. A hybrid RANS-LES approach with delayed-DES and wall-modelled LES capabilities. *International Journal of Heat and Fluid Flow*, 29(6):1638-1649. https://doi.org/10.1016/j.ijheatfluidflow.2008.07.001

Spalart PR, Deck S, Shur ML, et al., 2006. A new version of detached-eddy simulation, resistant to ambiguous grid densities. *Theoretical and Computational Fluid Dynamics*, 20(3):181-195. https://doi.org/10.1007/s00162-006-0015-0

Tian HQ, 2007. Train Aerodynamics. China Railway Publishing House, Beijing, China (in Chinese).

Wang JB, Minelli G, Dong TY, et al., 2019. The effect of bogie fairings on the slipstream and wake flow of a high-speed train. An IDDES study. *Journal of Wind Engineering and Industrial Aerodynamics*, 191:183-202. https://doi.org/10.1016/j.jweia.2019.06.010

Wang SB, Bell JR, Burton D, et al., 2017. The performance of different turbulence models (URANS, SAS and DES) for predicting high-speed train slipstream. *Journal of Wind Engineering and Industrial Aerodynamics*, 165:46-57. https://doi.org/10.1016/j.jweia.2017.03.001

Wang SB, Burton D, Herbst A, et al., 2018. The effect of bogies on high-speed train slipstream and wake. *Journal of Fluids and Structures*, 83:471-489. https://doi.org/10.1016/j.jfluidstructs.2018.03.013

Xia C, Wang HF, Shan XZ, et al., 2017. Effects of ground configurations on the slipstream and near wake of a high-speed train. *Journal of Wind Engineering and Industrial Aerodynamics*, 168:177-189. https://doi.org/10.1016/j.jweia.2017.06.005

Yan LG, 2007. The maglev development and commercial application in China. International Conference on Electrical Machines and Systems, p.541-548.

Zhang L, Zhang JY, Li T, et al., 2017. Multi-objective aerodynamic optimization design of high-speed train head shape. *Journal of Zhejiang University-SCIENCE A (Applied Physics & Engineering)*, 18(11):841-854. https://doi.org/10.1631/jzus.A1600764

Zhou P, Zhang JY, Li T, 2020. Effects of blocking ratio and Mach number on aerodynamic characteristics of the evacuated tube train. *International Journal of Rail Transportation*, 8(1):27-44. https://doi.org/10.1080/23248378.2019.1675191

中文概要

题　目：新型高速磁浮车绕流特性的数值模拟研究

目　的：通过对新型高速磁浮车的绕流进行数值模拟，研究气动荷载、涡流及滑流的分布规律，为常导高速磁浮车的研发和应用奠定一定的气动基础。

创新点：1. 将可压缩流动理论及延时分离涡（IDDES）方法应用于高速磁浮车气动问题；2. 通过数值模拟，首次揭示高速磁浮车诱发的涡流特性。

方　法：1. 基于 430 km/h 的磁浮车气动试验数据，验证本文数值方法的可靠性，并建立三编组新型高速磁浮车的计算模型；2. 采用 IDDES 方法对关键问题即湍流求解进行建模，以捕捉较为精细的流场结构；3. 采用时均化和快速傅里叶变换等方法对流场数据进行后处理，以研究流场的时均和频率等特性。

结　论：1. 新型高速磁浮车具有良好的气动性能，比如较小的阻力系数、合理的升力系数和分散性较好的气动力主频分布。2. 在非流线型车身附近，两对反向旋转的大涡使得边界层明显增厚。3. 高强度的涡流主要分布在裙板与轨道以及轨道与车底之间的狭小空间；在轨道与车底之间（除了靠近尾车鼻尖附近的区域），涡脱频域几乎不变，且涡强沿流向指数式增大。4. 伴随着涡流的分裂及衍生，尾流具有复杂的、随机的频域分布特性。5. 高速磁浮车产生的时均滑流具有 5 个典型的变化过程。

关键词：磁浮车；高速；IDDES；气动荷载；涡流；时均滑流